

Advancing quantum process tomography through universal compilation

Huynh Le Dan Linh^{1,2}, Vu Tuan Hai³, and Le Bin Ho^{4,5,*}

¹University of Information Technology, Ho Chi Minh City, 700000, Vietnam

²Vietnam National University, Ho Chi Minh City, 700000, Vietnam

³Nara Institute of Science and Technology, 8916-5 Takayama-cho, Ikoma, Nara 630-0192, Japan

⁴Frontier Research Institute for Interdisciplinary Sciences, Tohoku University, Sendai 980-8578, Japan

⁵Department of Applied Physics, Graduate School of Engineering, Tohoku University, Sendai 980-8579, Japan

*binho@fris.tohoku.ac.jp

ABSTRACT

Quantum process tomography (QPT) is crucial for characterizing operations in quantum gates and circuits, however, existing methods face scalability and noise sensitivity challenges. Here, we propose a QPT approach based on universal compilation, which systematically decomposes quantum processes into optimized Kraus operators and Choi matrices. This method utilizes efficient algorithms to improve accuracy while reducing resource requirements. We benchmark our approach through numerical simulations of random unitary gates, demonstrating highly accurate quantum process characterization. Additionally, we apply it to dephasing processes with time-homogeneous and time-inhomogeneous noise, achieving improved fidelity and robustness. Our work further enables broader applications in quantum error correction and device validation.

Quantum process tomography (QPT) is a technique used to characterize unknown quantum processes¹⁻³. A standard approach involves preparing a set of quantum states, applying the process, and then reconstructing the output states using quantum state tomography¹. QPT is crucial for verifying and characterizing the operations of quantum gates and circuits^{2,4-7}. However, efficiency and computational complexity remain significant challenges, particularly as the system size increases^{8,9}. The direct implementation of QPT typically scales exponentially, making it impractical for large-scale quantum systems^{10,11}. As quantum technologies continue to advance, it is essential to develop more efficient methods to improve precision while reducing the computational cost of QPT.

Recent advancements have aimed to improve the efficiency of QPT. For example, Ahmed et al.¹² proposed a machine learning-based approach that optimizes a set of Kraus operators using Riemannian gradient descent, enabling efficient characterization of quantum processes through iterative adjustments. Building on this, Daniel et al.¹³ demonstrated that Riemannian gradient descent accelerates the optimization of quantum processes by leveraging the structure of the parameter space through Riemannian geometry¹⁴. These approaches highlight the po-

tential of machine learning and advanced optimization techniques to enhance QPT efficiency^{11,15,16}. However, despite these improvements, the approach remains computationally expensive due to the large number of measurements required, as the tomography step still relies on standard QPT methods.

In this work, we introduce a quantum compilation-based QPT (CQPT) framework, which integrates universal compilation techniques^{17,18} with QPT methods to optimize the tomography process, minimizing computational costs while maintaining high precision.

A standard quantum compilation mainly converts target unitaries into trainable unitaries, enabling applications like gates optimization¹⁹, quantum-assisted compiling²⁰, continuous-variable targets²¹, quantum state tomography¹⁷, and quantum dynamics simulation²². In CQPT, we extend the target unitaries to quantum processes, and the trainable unitaries become trainable Kraus operators or Choi matrices.

The core innovation of this framework is the application of quantum compilation, a quantum machine learning technique, to optimize QPT, thereby reducing the complexity of traditional QPT methods. This approach makes QPT scalable and practical for larger quantum systems, addressing a fundamental

limitation of existing methods.

To achieve this, we build two key theorems. The first theorem focuses on the optimization of Kraus operators through quantum compilation, while the second presents a similar framework for Choi matrices. The Kraus operators representation is crucial for characterizing unitary processes, as it enables a direct description of the quantum channel in terms of experimentally determinable operators. Similarly, the Choi matrices offer a compact representation of a quantum operation, which is particularly valuable for understanding the behavior of quantum channels, especially in noisy environments like open quantum systems.

We then demonstrate the practical application of these theorems in several quantum processes, including random unitary processes, dephasing processes, and quantum systems affected by both time-homogeneous and time-inhomogeneous noises. To optimize in the CQPT, we employ the Riemannian gradient descent method. This approach ensures that the estimation process not only minimizes computational cost but also accounts for the geometry of the quantum process space, leading to a more accurate and efficient tomography process.

Through numerical simulations and analytical derivations, we demonstrate that our CQPT method significantly enhances efficiency and reduces the computational complexity of quantum process tomography, making it practical for large-scale quantum systems. Our approach holds promise for both fundamental quantum information research and practical applications, such as quantum computing and communication, where precise process characterization is essential.

Results

Universal compilation-based quantum process tomography framework

QPT is a method for fully characterizing an unknown quantum process \mathcal{E} , modeled as a completely positive and trace-preserving (CPTP) map. The process can be expressed in the operator-sum representation $\mathcal{E}(\rho) = \sum_l K_l \rho K_l^\dagger$, where K_l are Kraus operators satisfying $\sum_l K_l^\dagger K_l = \mathbf{I}$. Alternatively, QPT represents \mathcal{E} through its Choi matrix $\mathbf{J}_{\mathcal{E}}$, an operator spanning on $H_{\mathcal{X}} \otimes H_{\mathcal{Y}}$, ie., $\mathcal{E}(\rho) = \text{Tr}_{\mathcal{X}}[(\rho^\top \otimes \mathbf{I}) \mathbf{J}_{\mathcal{E}}]$. This matrix is constructed using the Choi-Jamiolkowski

isomorphism as $\mathbf{J}_{\mathcal{E}} = \sum_{i,j} |i\rangle\langle j| \otimes \mathcal{E}(|i\rangle\langle j|)$ where $\{|i\rangle\}$ is an orthonormal basis. In an N -qubit system, the Hilbert space dimension is 2^N , $K_l \in \mathbb{C}^{2^N \times 2^N}$, and $\mathbf{J}_{\mathcal{E}} \in \mathbb{C}^{4^N \times 4^N}$.

Experimentally, QPT involves preparing input states $\{\rho_i\}$, applying \mathcal{E} , and measuring the outputs using a positive operator-valued measure (POVM) $\{M_j\}$. The collected data are used to extract Kraus operators or reconstruct $\mathbf{J}_{\mathcal{E}}$ through inversion^{1,2}, estimation methods^{15,23–26}, or optimization techniques^{11,15,16}. QPT is essential for validating quantum gates^{7,27}, benchmarking devices⁷, and analyzing noise in quantum systems⁷.

In this work, we present a compilation-based approach for quantum process tomography (CQPT). In the standard compilation, two unitary operators, U and $V(\boldsymbol{\theta})$, are used, where $V(\boldsymbol{\theta})$ is optimized through parameters $\boldsymbol{\theta}$ to satisfy $V^\dagger(\boldsymbol{\theta})U = \mathbf{I}e^{i\phi}$ for any ϕ . Here, we extend U to a CPTP process \mathcal{E} , and generalize $V(\boldsymbol{\theta})$ to a set of k Kraus operators $\mathbf{k} = (K_1, K_2, \dots, K_k)^\top$, $\mathbf{k}^\dagger \mathbf{k} = \mathbf{I}$, where $\mathbf{k}^\dagger \mathbf{k} = \mathbf{I}$ and K_l are optimizable Kraus operators. The CQPT is then defined as follows.

Theorem 1. (Kraus-based CQPT) *A set of trainable Kraus operators $\mathbf{k} = (K_1, \dots, K_k)^\top$, $\mathbf{k}^\dagger \mathbf{k} = \mathbf{I}$, represents a quantum process \mathcal{E} , which is a fully invertible CPTP map, if the following condition holds*

$$\rho_f \equiv \mathcal{E}^{-1} \left(\sum_{l=1}^k K_l \rho_{in} K_l^\dagger \right) = \rho_{in}, \quad (1)$$

where $\rho_{in(f)}$ is the initial (final) state, \mathcal{E}^{-1} is the inverse process of \mathcal{E} .

Proof. For an initial quantum state ρ_{in} , its evolution under the process \mathcal{E} is given by $\rho_{\mathcal{E}} = \mathcal{E}(\rho_{in})$. Alternatively, the evolved state can be expressed using Kraus operators as $\rho_{\mathbf{k}} = \sum_l K_l \rho_{in} K_l^\dagger$. The Kraus operators \mathbf{k} represent \mathcal{E} if $\rho_{\mathcal{E}} = \rho_{\mathbf{k}}$, which implies $\sum_l K_l \rho_{in} K_l^\dagger = \mathcal{E}(\rho_{in})$. Applying the inverse process \mathcal{E}^{-1} to both sides gives $\rho_f \equiv \mathcal{E}^{-1} \left(\sum_l K_l \rho_{in} K_l^\dagger \right) = \rho_{in}$. Thus, \mathbf{k} is a valid representation of \mathcal{E} . \square

Remark 1. (Unitary processes) If \mathcal{E} is a unitary process, ie., $\mathcal{E}(\rho) = U \rho U^\dagger$ for some unitaries U , then $\mathcal{E}^{-1}(\rho) = U^\dagger \rho U$. This approach is crucial for validating quantum gates and benchmarking quantum devices.

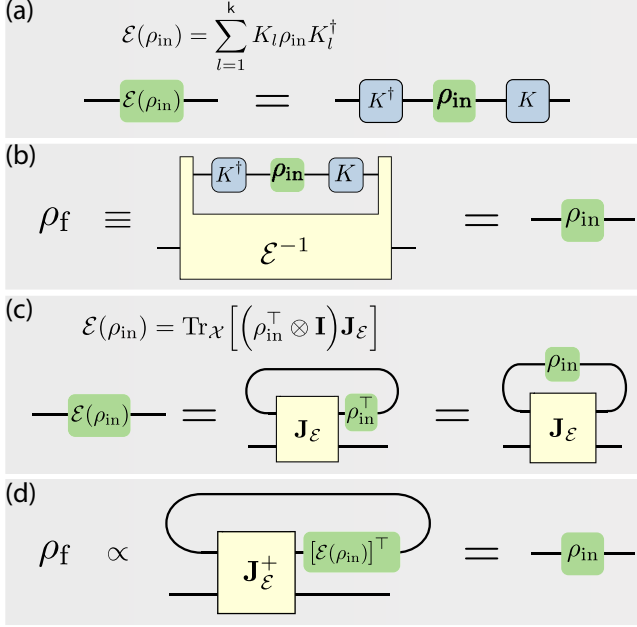


Figure 1. Graphical presentation. (a) Quantum channel representation with Kraus operators. (b) Visualization of Theorem 1. (c) Quantum channel representation using the Choi matrix. (d) Visualization of Theorem 2.

For example, to validate a quantum gate U using Kraus operators, we start with an initial quantum state ρ_{in} and apply Kraus operators \mathbf{k} to the state, yielding $\sum K_l \rho_{\text{in}} K_l^\dagger$. We then apply the inverse process, which corresponds to applying the inverse U operator U^\dagger , giving $U^\dagger \sum_l (K_l \rho_{\text{in}} K_l^\dagger) U$. By iteratively optimizing \mathbf{k} to minimize the difference between the recovered and initial states, we refine \mathbf{k} until it converges to the unitary operator U representing the quantum gate.

Figure 1 (a) illustrates a quantum channel where the initial state ρ_{in} is transformed by a set of Kraus operators. Figure 1 (b) visualizes Theorem 1, showing that after applying the Kraus operators, the inverse operator \mathcal{E}^{-1} is performed. The final state ρ_f returns to ρ_{in} when $\sum_l K_l \rho_{\text{in}} K_l^\dagger = \mathcal{E}(\rho_{\text{in}})$.

Previous studies^{12,13} optimize \mathbf{k} by comparing $\rho_{\mathcal{E}}$ and $\rho_{\mathbf{k}}$, i.e., minimizing a cost function $C(\mathbf{k}) = \sum_{ij} \left(\text{Tr}[M_j(\rho_{\mathcal{E}}^i - \rho_{\mathbf{k}}^i)] \right)^2$, where $i \in [1, \mathbf{n}]$ for \mathbf{n} different input states $\rho_{\text{in}}^1, \dots, \rho_{\text{in}}^{\mathbf{n}}$, and $j \in [1, \mathbf{p}]$ corresponds to \mathbf{p} elements in the POVM. This method is costly because it requires full measurements of the POVM M .

In our CQPT framework, we employ a quantum compilation process that benefits from “single-shot” measurements^{17,28}. Starting with an initial pure state $|\psi\rangle$, we apply the trainable Kraus operators \mathbf{k} followed by \mathcal{E}^{-1} , which yields the final state $\rho_f = \mathcal{E}^{-1} \left(\sum_l K_l |\psi\rangle\langle\psi| K_l^\dagger \right)$. The cost function $C(\mathbf{k})$ is defined through the infidelity

$$C(\mathbf{k}) = 1 - \int_{\psi} \left| \text{Tr}[\rho_f |\psi\rangle\langle\psi|] \right|^2 = 1 - \int_{W \in \text{Haar}} \left| \text{Tr}[W^\dagger \rho_f W |\mathbf{0}\rangle\langle\mathbf{0}|] \right|^2, \quad (2)$$

where we used $|\psi\rangle = W|\mathbf{0}\rangle$ for an arbitrary random unitary W and $|\mathbf{0}\rangle \equiv |00\dots 0\rangle$ is the initial state in a quantum register.

Practically, in the quantum register, we first prepare N qubits initialized by $|00\dots 0\rangle$, apply W , followed by \mathbf{k} and \mathcal{E}^{-1} , and apply W^\dagger again. Then, we measure the final state on the basis $|\mathbf{0}\rangle$ and obtain the probability $p(00\dots 0) = \text{Tr}[W^\dagger \rho_f W |\mathbf{0}\rangle\langle\mathbf{0}|]$, which is used for optimization. This method is known as single-shot measurement, where we only need the probability of the classical outcome $00\dots 0$, see also Refs.^{17,28}. We also replace $W \in \text{Haar}$ by $W = \{W_i, \forall i \in [1, \mathbf{n}]\}$, i.e., \mathbf{n} input states. The model is trained by updating \mathbf{k} iteratively until $C(\mathbf{k}) \approx 0$, ensuring that \mathbf{k} optimally represents the Kraus operators for the quantum channel \mathcal{E} .

To optimize the cost function, we apply the Riemannian optimization method^{12–14} and use the gradient descent on the cost function $C(\mathbf{k})$, defined on a Riemannian manifold. The Riemannian gradient is derived by projecting the Euclidean gradient onto the tangent space as

$$\text{grad}C(\mathbf{k}) = \nabla C(\mathbf{k}) - \mathbf{k} \text{Sym}(\mathbf{k}^\dagger \nabla C(\mathbf{k})), \quad (3)$$

where $\text{Sym}(\mathbf{A}) = (\mathbf{A} + \mathbf{A}^\dagger)/2$. Here, we use ‘grad’ for the Riemannian gradient and ‘ ∇ ’ for the Euclidean gradient. Using the Riemannian gradient descent, we update \mathbf{k} iteratively

$$\mathbf{k}_{t+1} = \text{Retract}_{\mathbf{k}}[-\alpha \text{grad}C(\mathbf{k})], \quad (4)$$

where α is the learning rate, and the retraction ensures the update remains on the manifold. We apply an iterative Cayley transformation for the retraction, which approximates a second-order mapping of a tangent vector onto the manifold²⁹. Further details are provided in the Methods section.

Remark 2. (Irreversible processes) Some quantum channels are irreversible, e.g., the depolarizing channel, causing information loss and making ρ_{in} unrecoverable. To address this, we introduce the following theorem for the CQPT, based on Choi matrices.

Theorem 2. (Choi-based CQPT) A trainable Choi matrix $\mathbf{J}_{\mathcal{E}}$ is a $4^N \times 4^N$ positive semi-definite matrix that satisfies $\text{Tr}_{\mathcal{Y}}(\mathbf{J}_{\mathcal{E}}) = \mathbf{I}$. It represents a quantum process \mathcal{E} , which is a CPTP map, if the following condition holds

$$\rho_f \propto \text{Tr}_{\mathcal{X}} \left[\left([\mathcal{E}(\rho_{\text{in}})]^\top \otimes \mathbf{I} \right) \mathbf{J}_{\mathcal{E}}^+ \right] = \rho_{\text{in}}, \quad (5)$$

where $\mathbf{J}_{\mathcal{E}}^+$ is the pseudoinverse of $\mathbf{J}_{\mathcal{E}}$, and $\text{Tr}_{\mathcal{X}(\mathcal{Y})}$ represents the partial trace over the Hilbert space $H_{\mathcal{X}(\mathcal{Y})}$. The proportionality accounts for a normalization factor in ρ_f .

See Fig. 1 (c, d) for a graphical illustration of the Choi-based quantum process and Theorem (2).

Proof. See detailed in the Methods. \square

Remark 3. (Cost function and training process). Similar previous section, the cost function $C(\mathbf{J}_{\mathcal{E}})$ is defined through the infidelity

$$C(\mathbf{J}_{\mathcal{E}}) = 1 - \int_{W \in \text{Haar}} \left| \text{Tr} \left[\left(\mathcal{E}(\rho_{\text{in}})^\top \otimes \rho_{\text{in}} \right) \mathbf{J}_{\mathcal{E}}^+ \right] \right|^2, \quad (6)$$

where $\rho_{\text{in}} = W|\mathbf{0}\rangle\langle\mathbf{0}|W^\dagger$ for an arbitrary random unitary W .

Proof. See detailed in the Methods. \square

The training process begins by initializing an N -qubit system in the Hilbert space $H_{\mathcal{X}}$ in state $|00\cdots 0\rangle$. The operator W is applied, followed by the quantum channel \mathcal{E} and a sequence of SWAP gates to obtain $\mathcal{E}(\rho_{\text{in}})^\top$. The same ρ_{in} is prepared in another N -qubit system within the Hilbert space $H_{\mathcal{Y}}$. The joint system $H_{\mathcal{X}} \otimes H_{\mathcal{Y}}$ then undergoes the application of $\mathbf{J}_{\mathcal{E}}^+$. Finally, W^\dagger is applied to the $H_{\mathcal{Y}}$ subspace, and the output state is measured in the $|\mathbf{0}\rangle$ basis, resulting in the probability $p(00\cdots 0)$. To optimize $\mathbf{J}_{\mathcal{E}}$, we minimize $C(\mathbf{J}_{\mathcal{E}})$ until it converges, ensuring that $\mathbf{J}_{\mathcal{E}}$ accurately represents the Choi matrix of the quantum channel \mathcal{E} . Further details are provided in Fig. 11 in the Methods section.

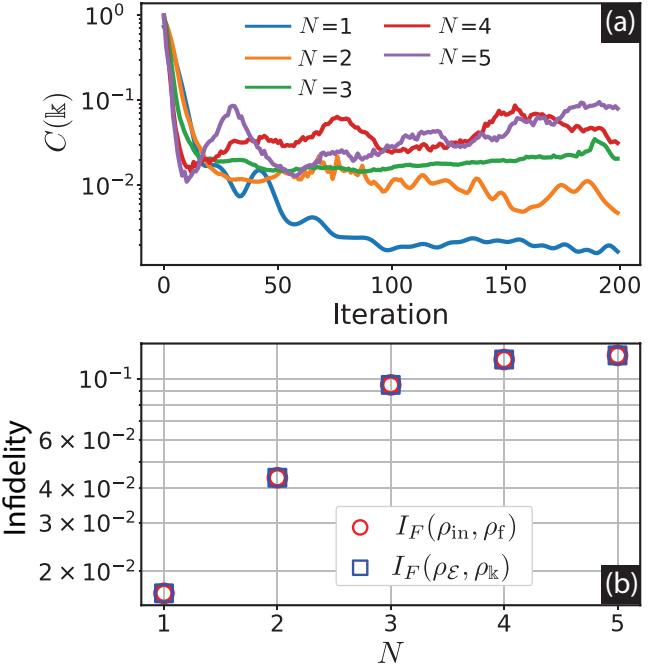


Figure 2. Benchmarking Haar random unitary gates. (a) Convergence of the cost function $C(\mathbb{k})$ over iterations. (b) Average infidelity as a function of the qubit numbers N .

Benchmarking Haar random unitary quantum gates

In this section, we apply CQPT to benchmark Haar random unitary quantum gates. Given a process $\mathcal{E} \equiv U_{\text{Haar}}$, a Haar random unitary gate³⁰, we construct trainable Kraus operators $\mathbb{k} = (K_1, K_2, \dots, K_{\mathbb{k}})^\top$. We have $\rho_{\mathcal{E}} = U_{\text{Haar}} \rho_{\text{in}} U_{\text{Haar}}^\dagger$, and $\rho_{\mathbb{k}} = \sum_{l=1}^{\mathbb{k}} K_l \rho_{\text{in}} K_l^\dagger$, where $\rho_{\text{in}} = W|\mathbf{0}\rangle\langle\mathbf{0}|W^\dagger$. Following Theorem 1, the final state yields

$$\rho_f = U_{\text{Haar}}^\dagger \left(\sum_{l=1}^{\mathbb{k}} K_l \rho_{\text{in}} K_l^\dagger \right) U_{\text{Haar}}. \quad (7)$$

To optimize \mathbb{k} , we generate 6^N random input states ρ_{in} and use a single measurement, $M = |\mathbf{0}\rangle\langle\mathbf{0}|$, for training^{12, 31}. For testing, we generate another set of 6^N random input states. In general, both the training and testing sets can be selected arbitrarily. The cost function in Eq. (2) is evaluated by approximating the integral with a summation over the training set. \mathbb{k} is then iteratively updated using Eq. (4) until convergence. In our implementation, we use the number of Kraus terms $\mathbb{k} = 2^N \ll 4^N$ (full-rank process). All numerical simulations are performed on a workstation equipped with an Intel

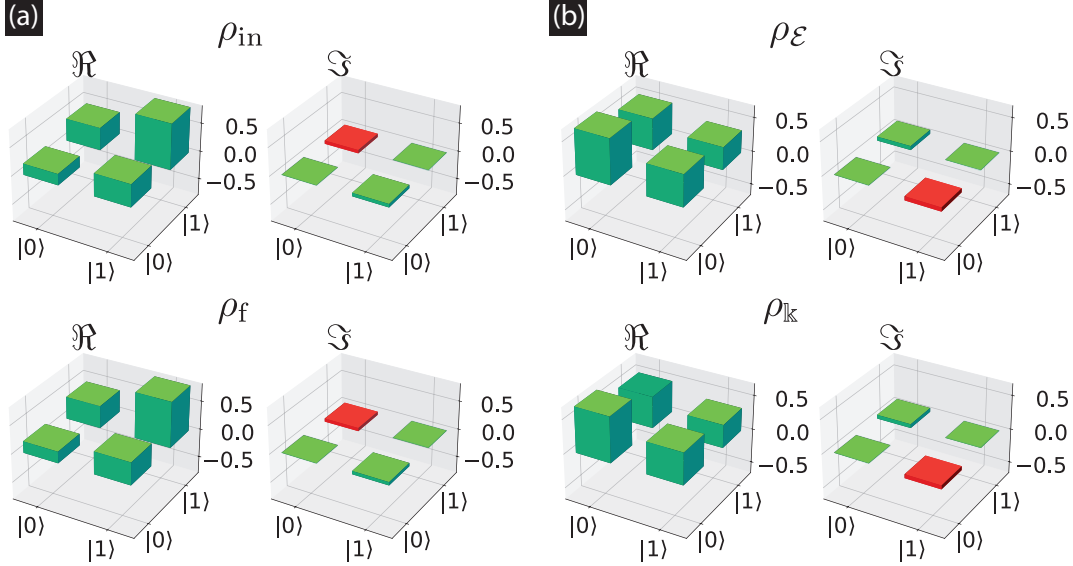


Figure 3. Benchmarking Haar random unitary gates. (a) Comparison of an initial and final states, ρ_{in} and ρ_f , where ρ_{in} is selected from the testing set. Here, \Re and \Im denote the real and imaginary parts, respectively. Green indicates positive values, while red represents negative values. (b) Comparison of intermediate quantum states ρ_E and ρ_k to evaluate transformation accuracy.

Core i9-10920X processor (128 GB of RAM) and a GPU A6000.

Figure 2(a) shows the cost function over iterations for different N . In general, the cost function gradually decreases, which indicates effective learning of the quantum channel. As N increases, the convergence rate slows and thus requires more iterations to minimize.

Figure 2(b) compares the average infidelity across different N . The infidelity between quantum states ρ and σ is given by

$$I_F(\rho, \sigma) = 1 - \text{Tr}(\sqrt{\sqrt{\rho}\sigma\sqrt{\rho}}), \quad (8)$$

where lower values indicate higher similarity.

We evaluate the average infidelities $I_F(\rho_{in}, \rho_f)$ and $I_F(\rho_E, \rho_k)$ over 6^N testing states. The results show that both infidelities closely match and increase with N , suggesting that while the transformation remains accurate, deviations accumulate as N grows. Additionally, numerical imprecision and optimization limits introduce minor but unavoidable errors, gradually increasing infidelity.

Figure 3 compare density matrices for $N = 1$. A random state ρ_{in} is chosen from the testing set, and its evolution to ρ_f is shown in Fig. 3(a), demonstrating a consistent quantum transformation. Likewise,

Fig. 3(b) compares ρ_E and ρ_k , showing strong agreement, which confirms that the optimized quantum channel k effectively reconstructs the target process \mathcal{E} . The close match in both cases validates the accuracy of the reconstruction and the reliability of the method.

Dephasing noise process

Dephasing noise is a process that gradually erases coherence between quantum states due to environmental interactions. In multi-qubit systems, each qubit dephases independently, affecting phase information while preserving state populations. The dephasing process for a qubit j is given by

$$\mathcal{E}_j(\rho) = \frac{1 + \sqrt{1 - \gamma}}{2} \rho + \frac{1 - \sqrt{1 - \gamma}}{2} \sigma_z \rho \sigma_z, \quad (9)$$

where ρ is the qubit state, σ_z is the Pauli-Z operator, and $\gamma \in [0, 1]$ is the noise strength. At $\gamma = 0$, there is no noise, and as γ increases, decoherence drives the state toward a maximally mixed state.

The total dephasing process on an N -qubit system is given by the product of the dephasing operations on each qubit

$$\mathcal{E}_{\text{total}}(\rho) = \prod_{j=1}^N \mathcal{E}_j(\rho). \quad (10)$$

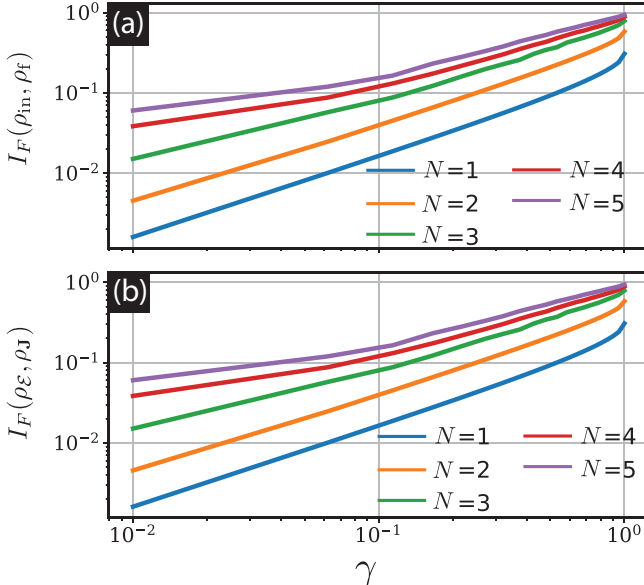


Figure 4. CQPT for dephasing noise process.

(a) Average infidelity $I_F(\rho_{\text{in}}, \rho_{\text{f}})$ versus γ . (b) Average infidelity $I_F(\rho_{\mathcal{E}}, \rho_{\mathbf{J}})$ versus γ , showing the effect of noise on optimization performance.

To perform quantum process tomography, we employ the Choi-based CQPT method. The process begins with the initial state $\rho_{\text{in}} = W|\mathbf{0}\rangle\langle\mathbf{0}|W^\dagger$, which evolves under the map $\rho_{\mathcal{E}} = \mathcal{E}_{\text{total}}(\rho_{\text{in}})$. To reconstruct $\mathcal{E}_{\text{total}}$, we optimize a variational Choi matrix $\mathbf{J}_{\mathcal{E}}$, which is initially generated randomly. The training procedure involves generating 6^N initial states ρ_{in} and evaluating the cost function as defined in Eq. (6). When the cost function $C(\mathbf{J}_{\mathcal{E}})$ reaches minimum, we obtain the reconstructed state $\rho_{\mathbf{J}} \approx \rho_{\mathcal{E}}$, where $\rho_{\mathbf{J}} = \text{Tr}_{\mathcal{X}}[(\rho_{\text{in}}^\top \otimes \mathbf{I})\mathbf{J}_{\mathcal{E}}]$.

We evaluate the efficiency at different noise levels by calculating the average infidelity $I_F(\rho_{\text{in}}, \rho_{\text{f}})$ and $I_F(\rho_{\mathcal{E}}, \rho_{\mathbf{J}})$ over 6^N random states from the testing set. Fig. 4 shows that for small noise parameters γ , the optimized $\mathbf{J}_{\mathcal{E}}$ accurately recovers the dephasing process. As γ increases, the recovery becomes less precise, leading to a larger discrepancy between the reconstructed and target states. Despite this, even for larger N , the process remains effectively learned, although it becomes more challenging. These results show that higher noise levels and larger systems increase the complexity of the learning process, thereby reducing the accuracy of process tomography.

We further compare the evolved density matrices

$\rho_{\mathcal{E}}$ and $\rho_{\mathbf{J}}$ for $N = 1$ for low noise ($\gamma = 0.01$) and high noise ($\gamma = 1.0$). As shown in Fig. 5 at low noise levels, the two states match closely each other for both real and imaginary parts. However, as the noise level increases, the difference between $\rho_{\mathcal{E}}$ and $\rho_{\mathbf{J}}$ becomes more pronounced, which can be seen clearly in the imaginary part, implying reduced accuracy in the reconstruction.

Time-homogeneous and time-inhomogeneous noises

In quantum systems, noise can be categorized by how it changes over time. The following cases describe two types of dephasing noise, defined through

$$\gamma = \begin{cases} 1 - e^{-2\beta t}, & \text{time-homogeneous} \\ 1 - e^{-\beta t^2}, & \text{time-inhomogeneous,} \end{cases} \quad (11)$$

where t represents time, and β denotes the dephasing rate. The noise strength γ increases from 0 at $t = 0$ to 1 at $t \rightarrow \infty$.

The first case represents time-homogeneous noise, where the noise strength increases exponentially over time. The noise rate remains constant, leading to a Markovian process where the noise evolution depends only on the current state. Such behavior is typical of many natural decay processes, such as thermal dephasing or spontaneous emission, where the loss of coherence occurs steadily over time.

In contrast, the second case describes time-inhomogeneous noise. Here, the noise follows a quadratic time dependence, growing slowly at first and then accelerating as time progresses. This results in a non-Markovian process, where the rate of dephasing varies over time and retains some memory of past states. This behavior is typical of systems with diffusive noise or time-dependent fluctuations.

We first reconstruct the time-dependent states $\rho_{\mathcal{E}}(t)$ and $\rho_{\mathbf{J}}(t)$ for both noise cases using the CQPT. We then calculate the expectation value $\langle \sigma_x(t) \rangle$, given by

$$\langle \sigma_x(t) \rangle_{\mathcal{E}} = \text{Tr}[\sigma_x \rho_{\mathcal{E}}(t)], \quad (12)$$

$$\langle \sigma_x(t) \rangle_{\mathbf{J}} = \text{Tr}[\sigma_x \rho_{\mathbf{J}}(t)]. \quad (13)$$

For simplicity, we focus on a 1-qubit system and set $\beta = 0.1$ in the numerical example.

Figure 6 displays the expectation values over time for both time-homogeneous and time-inhomogeneous

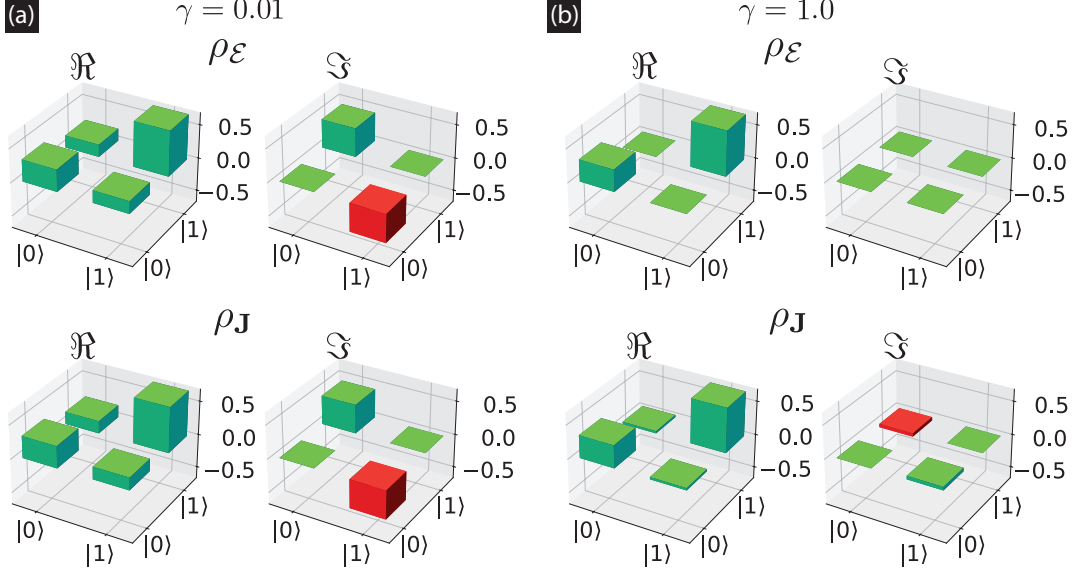


Figure 5. CQPT for dephasing noise process. (a) Comparison of quantum states ρ_E and ρ_J at $\gamma = 0.01$, demonstrating a close match. (b) Comparison at $\gamma = 1.0$, highlighting the growing discrepancy between the quantum states with higher noise.

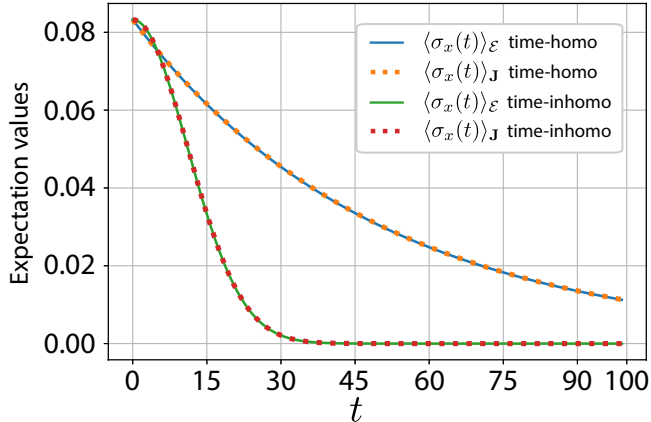


Figure 6. Expectation values. Plot of the expectation value $\langle \sigma_x(t) \rangle_X$, where $X = \mathcal{E}$ represents the quantum state $\rho_E(t)$ and $X = \mathbf{J}$ represents $\rho_J(t)$. The plot compares time-homogeneous and time-inhomogeneous noise cases.

noise, comparing the true evolved state with the reconstructed process. For time-homogeneous noise, the expectation values decay exponentially, indicating constant-rate decoherence typical of Markovian processes like thermal dephasing. In contrast, for time-inhomogeneous noise, the decay starts slowly and then accelerates quadratically, reflecting a non-Markovian process, such as diffusive noise or time-

dependent fluctuations.

Comparison

We compare our approach with previous studies^{12,13} to assess its efficiency. These previous works utilize a Riemann gradient descent-based quantum process tomography method, which we also adopt for optimization. However, our training process differs significantly.

Previous studies, which we refer to as measurement-based QPT (MQPT), directly compare measurement outcomes between ρ_E and $\rho_{\mathbb{K}}$ using a cost function defined as

$$C(\mathbb{K}) = \sum_{ij} \left(\text{Tr} [M_j (\rho_E^i - \rho_{\mathbb{K}}^i)] \right)^2, \quad (14)$$

where $i \in [1, n]$ for n different input states $\rho_{in}^1, \dots, \rho_{in}^n$, and $j \in [1, p]$ corresponds to p elements in the POVM. In contrast, our approach—compilation-based QPT (CQPT)—incorporates a quantum compilation process for QPT, rather than direct state comparison. This key difference enables a more structured and potentially more efficient reconstruction of quantum processes.

We analyze an N -qubit system using a Haar random unitary process for comparison. The dataset consists of $n = 6^N$ initial states ρ_{in} . The MQPT

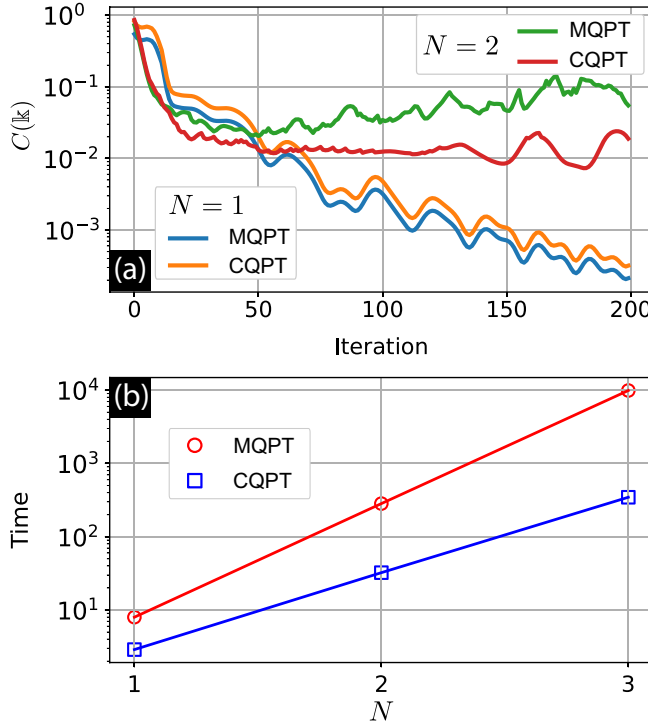


Figure 7. Comparing the MQPT and CQPT methods. (a) Cost function $C(k)$ versus the number of iterations for $N = 1$ and $N = 2$ qubits, comparing the two methods. (b) Execution time as a function of the number of qubits N for both methods.

method requires applying a measurement operator M with $p = 6^N$ measurements to each transformed state $\rho_{\mathcal{E}}$ and ρ_k ^{12,13}. This results in a total of $6^N \times 6^N$ measurements per learning iteration. Whereas, the CQPT method applies \mathcal{E} and k to ρ_{in} and requires only a single measurement per state, reducing the total to 6^N measurements per iteration.

Correspondingly, the total measurement time for the MQPT is

$$T_{MQPT} = c_1 \cdot (6^{2N}), \quad (15)$$

which grows rapidly with N , where c_1 is the time per measurement. For the CQPT, the measurement time is

$$T_{CQPT} = c_2 \cdot 6^N, \quad (16)$$

where c_2 is the measurement time per state. This follows a smaller exponential scaling, reducing computational cost.

As N increases, the CQPT becomes significantly more efficient. The MQPT doubles the required

measurements, increasing time complexity, while the CQPT eliminates unnecessary measurements, improving scalability for larger quantum systems.

Figure 7 presents the numerical results for different N . In Fig. 7(a), we compare the cost function convergence over iterations for $N = 1$ and $N = 2$. For $N = 1$, both methods show similar convergence speeds, but for $N = 2$, CQPT converges faster.

Figure 7(b) compares execution time. The CQPT significantly reduces the execution time compared to the MQPT. Moreover, as the number of qubits increases, the execution time in the CQPT grows at a slower rate, highlighting its efficiency.

For memory complexity, the MQPT requires storing both the process representation $\mathcal{O}(2^N \cdot 2^N)$ and extensive measurement outcomes, leading to $\mathcal{O}(4^N \cdot 6^N)$. The CQPT, by contrast, stores only the trainable operators $\mathcal{O}(4^N)$ and minimal final state data, achieving $\mathcal{O}(4^N)$. This efficiency, free from the 6^N dependent term, makes the CQPT significantly more memory-efficient and practical for large-scale quantum process tomography.

Discussion

We introduced a compilation-based quantum process tomography (CQPT) method optimized with Riemannian gradient descent. This approach models a quantum process using a sequence of trainable operators (such as Kraus operators or the Choi matrix) to extract process information efficiently. By ensuring the output state returns to its initial reference state, it avoids the need for full tomography or full-rank measurement bases, significantly reducing both measurement complexity and computational cost.

CQPT improves runtime efficiency compared to previous methods using the same Riemannian gradient descent^{12,13}. A key feature is that it uses single-shot measurements, eliminating the need for full-base measurements, i.e., tensor products of eigenvalues of Pauli matrices, and reducing overall measurement time. This makes CQPT highly practical for larger quantum systems and near-term quantum hardware with limited coherence times.

Furthermore, CQPT enhances precision by minimizing statistical errors or readout errors. It applies to both unitary and noisy quantum processes, making it a versatile tool for quantum gates validation, circuits benchmarking, and noise characterization.

However, CQPT has some limitations. While it can handle noisy quantum processes, extreme noise can still degrade accuracy. So far, state preparation and measurement (SPAM) errors remain a challenge in QPT. In our CQPT, single-shot measurements help minimize the measurement errors, however, state preparation errors can still affect the training process. Thus, additional error mitigation strategies may be required to improve robustness.

Despite these challenges, CQPT provides an efficient and accurate approach to QPT, making it a valuable tool for advancing quantum technologies.

Methods

Implementation of Kraus-based CQPT (Theorem 1)

The Kraus-based CQPT process begins by preparing a set of training quantum states, $\rho_{\text{in}}^{(i)} = W_i \rho_0 W_i^\dagger$ for $i \in [1, n]$, where ρ_0 serves as the reference state. The process then applies full-rank Kraus operators to evolve the initial state, followed by an inverse operation, \mathcal{E}^{-1} . Finally, applying W_i^\dagger restores the reference state ρ_0 . This approach is particularly effective when \mathcal{E} is invertible, such as in unitary processes.

For example, consider a random unitary process $\mathcal{E} = U$. We can also choose $\mathbb{k} = K$, a unitary operator. Theorem 1 gives

$$\begin{aligned} \rho_0 &\xrightarrow{W_i} W_i \rho_0 W_i^\dagger \xrightarrow{K} K(W_i \rho_0 W_i^\dagger) K^\dagger \\ &\xrightarrow{\mathcal{E}^{-1}} U^\dagger [K(W_i \rho_0 W_i^\dagger) K^\dagger] U \\ &\xrightarrow{W^\dagger} W^\dagger [U^\dagger [K(W_i \rho_0 W_i^\dagger) K^\dagger] U] W. \end{aligned} \quad (17)$$

The training is performed until $K = U$, then the final state becomes ρ_0 . Without loss of generality, we can fix ρ_0 to be a ground state or the computational basis state $|\mathbf{0}\rangle$. If $\rho_0 = |\mathbf{0}\rangle\langle\mathbf{0}|$, then measuring the final state in the basis $M_{\mathbf{0}}$ must yield $p_{\mathbf{0}} = 1$ for all W_i . To achieve optimal training, i.e., $K = U$, we define a cost function based on the average value of $p_{\mathbf{0}}$ over a random set of W_i , as given in Eq. (2). This CQPT scheme can be implemented in a quantum circuit, as illustrated in Fig. 8.

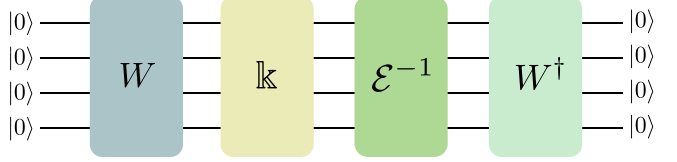


Figure 8. Implementation of the Kraus-based CQPT.

Implementation of Choi-based CQPT (Theorem 2)

Proof of Theorem 2

To prove Theorem 2, we assume that $\mathbf{J}_{\mathcal{E}}$ is the corrected Choi matrix representing \mathcal{E} and show that the left-hand side (LHS) and right-hand side (RHS) of Eq. (5) are equivalent.

First, we derive $\mathcal{E}(\rho_{\text{in}})$, where

$$\begin{aligned} \mathcal{E}(\rho_{\text{in}}) &= \text{Tr}_{\mathcal{X}} \left[(\rho_{\text{in}}^\top \otimes \mathbf{I}) \mathbf{J}_{\mathcal{E}} \right] \\ &= \sum_k \left(|k\rangle \otimes \mathbf{I} \right) \left[(\rho_{\text{in}}^\top \otimes \mathbf{I}) \mathbf{J}_{\mathcal{E}} \right] \left(|k\rangle \otimes \mathbf{I} \right) \\ &= \sum_k \mathbf{T}_k^\dagger \left[(\rho_{\text{in}}^\top \otimes \mathbf{I}) \mathbf{J}_{\mathcal{E}} \right] \mathbf{T}_k, \end{aligned} \quad (18)$$

where $\mathbf{T}_k = |k\rangle \otimes \mathbf{I} \in H_{\mathcal{X}} \otimes H_{\mathcal{Y}}$ for some orthogonal bases $\{|k\rangle\} \in H_{\mathcal{X}}$.

Next, we apply the vectorization on both sides of Eq. (18), which gives

$$\begin{aligned} \text{vec}[\mathcal{E}(\rho_{\text{in}})] &\stackrel{(a)}{=} \text{vec} \left[\sum_k \mathbf{T}_k^\dagger \left[(\rho_{\text{in}}^\top \otimes \mathbf{I}) \mathbf{J}_{\mathcal{E}} \right] \mathbf{T}_k \right] \\ &\stackrel{(b)}{=} \sum_k \text{vec} \left[\mathbf{T}_k^\dagger \left[(\rho_{\text{in}}^\top \otimes \mathbf{I}) \mathbf{J}_{\mathcal{E}} \right] \mathbf{T}_k \right] \\ &\stackrel{(c)}{=} \sum_k \left(\mathbf{T}_k^\top \otimes \mathbf{T}_k^\dagger \right) \text{vec} \left[(\rho_{\text{in}}^\top \otimes \mathbf{I}) \mathbf{J}_{\mathcal{E}} \right] \\ &\stackrel{(d)}{=} \sum_k \left(\mathbf{T}_k^\top \otimes \mathbf{T}_k^\dagger \right) \left(\mathbf{J}_{\mathcal{E}}^\top \otimes \mathbf{I} \right) \times \\ &\quad \text{vec} \left[(\rho_{\text{in}}^\top \otimes \mathbf{I}) \right] \\ &\stackrel{(e)}{=} \mathbf{J}_{\mathcal{E}}^\top \text{vec}[\rho_{\text{in}}^\top], \end{aligned} \quad (19)$$

where from (b) to (c) and from (c) to (d) we used $\text{vec}[ABC] = (C^\top \otimes A)\text{vec}[B]$ ³², and from (d) to (e) we applied computational basis $|k\rangle$ and simply ignored $H_{\mathcal{Y}}$. As a result, we have

$$\text{vec}[\mathcal{E}(\rho_{\text{in}})^\top] = \mathbf{J}_{\mathcal{E}} \text{vec}[\rho_{\text{in}}]. \quad (20)$$

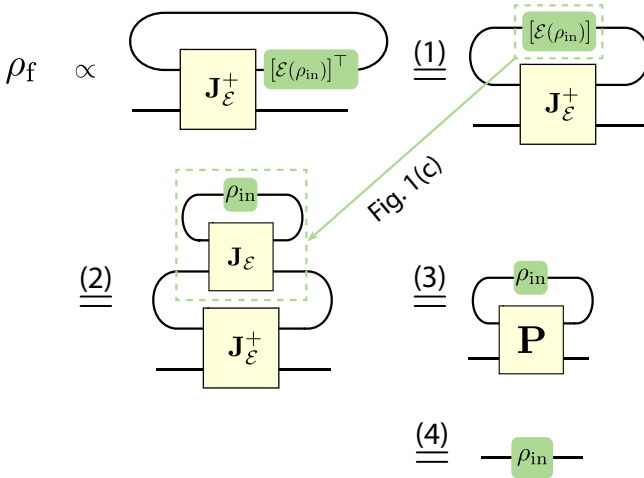


Figure 9. Graphical proof of Theorem 2.

Similarly, let the LHS of Eq. (5) be $\mathbf{L} = \text{Tr}_{\mathcal{X}}[(\mathcal{E}(\rho_{\text{in}})^{\top} \otimes \mathbf{I}) \mathbf{J}_{\mathcal{E}}^+]$, it gives

$$\text{vec}[\mathbf{L}] = (\mathbf{J}_{\mathcal{E}}^+)^{\top} \text{vec}[\mathcal{E}(\rho_{\text{in}})^{\top}]. \quad (21)$$

Substituting Eq. (20) into Eq. (21), we get

$$\begin{aligned} \text{vec}[\mathbf{L}] &= (\mathbf{J}_{\mathcal{E}}^+)^{\top} \mathbf{J}_{\mathcal{E}} \text{vec}[\rho_{\text{in}}] \\ &= \mathbf{P} \text{vec}[\rho_{\text{in}}] \\ &= \text{vec}[\rho_{\text{in}}] \equiv \text{vec}[\mathbf{R}], \end{aligned} \quad (22)$$

where we used $(\mathbf{J}_{\mathcal{E}}^+)^{\top} \mathbf{J}_{\mathcal{E}} = (\mathbf{J}_{\mathcal{E}}) \mathbf{J}_{\mathcal{E}}^+ = \mathbf{P}$ is a projection matrix, i.e., $\mathbf{P} \mathbf{X} = \mathbf{X}, \forall \mathbf{X}$, and $\mathbf{R} = \rho_{\text{in}}$, which stands for the RHS. As a result, Eq. (5) is proved.

Graphical proof of Theorem 2

In Fig. 9, we provide a graphical proof of Theorem 2. Starting from Fig. 1(d), we first transform $[\mathcal{E}(\rho_{\text{in}})]^{\top}$ into $[\mathcal{E}(\rho_{\text{in}})]$, then apply the operation in Fig. 1(c). Next, we replace $\mathbf{J}_{\mathcal{E}}^+ \mathbf{J}_{\mathcal{E}}$ with \mathbf{P} . Finally, since ρ_{in} is a projection operator, we recover ρ_{in} .

Proof of Remark 3

We proof that $\text{Tr}[(\mathcal{E}(\rho_{\text{in}})^{\top} \otimes \rho_{\text{in}}) \mathbf{J}_{\mathcal{E}}^+] = 1, \forall W$, when $\mathbf{J}_{\mathcal{E}}$ representing the Choi matrix for quantum channel \mathcal{E} . We start from

$$\text{Tr}[(A \otimes B)C] = \text{Tr}[\text{Tr}_{\mathcal{X}}[(A^{\top} \otimes \mathbf{I})C]B], \quad (23)$$

where $A \in H_{\mathcal{X}}, B \in H_{\mathcal{Y}}$ and $C \in H_{\mathcal{X}} \otimes H_{\mathcal{Y}}$. Apply to our case, we have

$$\begin{aligned} \text{Tr}[(\mathcal{E}(\rho_{\text{in}})^{\top} \otimes \rho_{\text{in}}) \mathbf{J}_{\mathcal{E}}^+] &\stackrel{(a)}{=} \text{Tr}_{\mathcal{Y}}[\text{Tr}_{\mathcal{X}}[(\mathcal{E}(\rho_{\text{in}})^{\top} \otimes \mathbf{I}) \mathbf{J}_{\mathcal{E}}^+] \rho_{\text{in}}] \\ &\stackrel{(b)}{=} \text{Tr}_{\mathcal{Y}}[\rho_{\text{in}} \rho_{\text{in}}] \\ &\stackrel{(c)}{=} 1, \end{aligned} \quad (24)$$

where from (a) to (b), we used Eq. (5), and from (b) to (c), we used the fact that ρ_{in} is a pure state, i.e., $W|\mathbf{0}\rangle$.

Graphical proof of Remark 3

We illustrate a graphical proof of Remark 3 in Fig. 10.

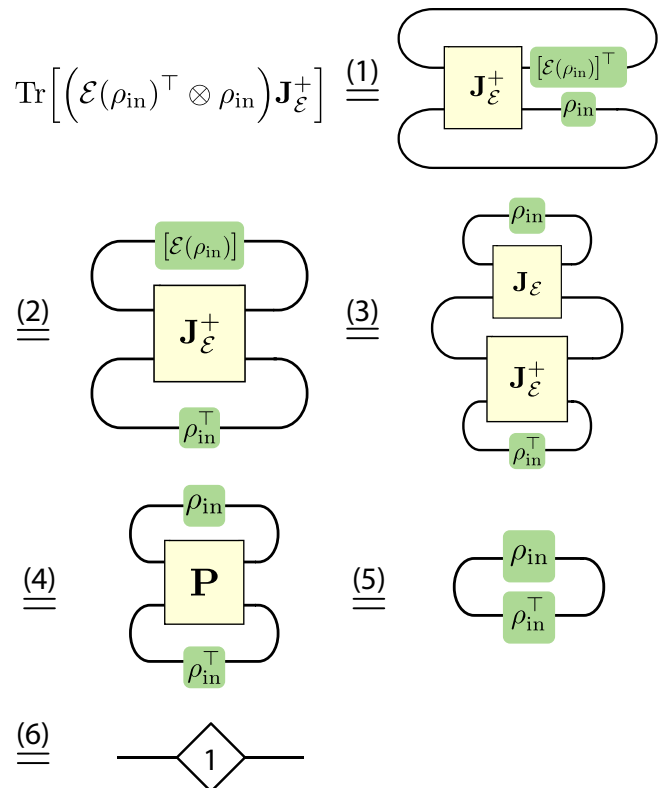


Figure 10. Graphical proof of Remark 3.

Quantum circuit-based implementation

To implement the cost function in Remark 3, we use a circuit-based measurement process, as illustrated in Fig. 11.

First, we prepare the pure state $\rho_{\text{in}} = W|\mathbf{0}\rangle$ in both $H_{\mathcal{X}}$ and $H_{\mathcal{Y}}$ subsystems. In $H_{\mathcal{X}}$, the state undergoes the quantum channel \mathcal{E} and a SWAP

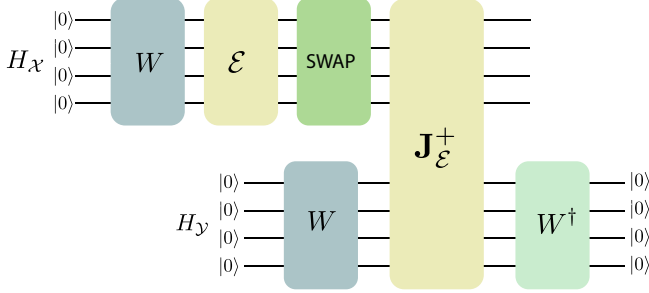


Figure 11. Implementation of the Choi-based CQPT.

gate, resulting in $\mathcal{E}(\rho_{\text{in}})^\top$. This leads to the joint state $\mathcal{E}(\rho_{\text{in}})^\top \otimes \rho_{\text{in}}$.

Next, we apply the pseudoinverse Choi matrix $\mathbf{J}_\mathcal{E}^+$ to the system. Finally, we apply W^\dagger to the H_Y subsystem and measure the probability p_0 of obtaining $|0\rangle$. By optimizing p_0 , we can refine the cost function to obtain the desired Choi matrix $\mathbf{J}_\mathcal{E}$.

Riemannian optimization

Consider the Stiefel manifold, which consists of all $d \times u$ unitary matrices $\mathcal{M}(d, u) = \{\mathbf{k} \in \mathbb{C}^{d \times u} \mid \mathbf{k}^\dagger \mathbf{k} = \mathbf{I}_u\}$. Here, \mathbf{k} is a $kd \times u$ matrix, with \mathbf{k} Kraus operators in our case. The tangent space $T_{\mathbf{k}}\mathcal{M}$ at any point \mathbf{k} consists of all matrices $\mathbf{V} \in \mathbb{C}^{d \times u}$ that satisfy $\mathbf{k}^\dagger \mathbf{V} + \mathbf{V}^\dagger \mathbf{k} = 0$. This ensures that small perturbations of \mathbf{k} remain on the Stiefel manifold.

For a curve $\gamma(\tau)$ on the manifold, the tangent vector is defined through the gradient $\mathbf{V} = \frac{d\gamma(\tau)}{d\tau} \Big|_{\tau=0}$. Since \mathbf{V} represents the gradient of our cost function, we write it as $\mathbf{V} = \text{grad}C(\mathbf{k})$. To ensure differentiability, we use the Riemannian manifold (\mathcal{M}, g) , where g is a smoothly varying inner product on the tangent space $g_{\mathbf{k}}(\mathbf{V}, \mathbf{W}) = \text{Tr}(\mathbf{V}^\dagger \mathbf{W})$. This leads to the geodesic equation $\gamma(t) = \text{Exp}_{\mathbf{k}}(\mathbf{V})$.

For optimization, we use gradient-based methods. Given a function $C : \mathcal{M}(d, u) \rightarrow \mathbb{R}$, the Riemannian gradient is obtained by projecting the Euclidean gradient onto the tangent space

$$\text{grad}C(\mathbf{k}) = \nabla C(\mathbf{k}) - \mathbf{k} \text{Sym}(\mathbf{k}^\dagger \nabla C(\mathbf{k})), \quad (25)$$

where $\text{Sym}(\mathbf{A}) = (\mathbf{A} + \mathbf{A}^\dagger)/2$. Using Riemannian gradient descent, we update \mathbf{k} iteratively:

$$\mathbf{k}_{t+1} = \text{Retract}_{\mathbf{k}}(-\alpha \text{grad}C(\mathbf{k})), \quad (26)$$

where α is the learning rate, and the retraction keeps the update on the manifold.

A retraction is a smooth mapping that approximates the exponential map while ensuring updates remain on the manifold $\text{Retract}_{\mathbf{k}} : T_{\mathbf{k}}\mathcal{M} \rightarrow \mathcal{M}$. It satisfies $\text{Retract}_{\mathbf{k}}(0) = \mathbf{k}$ and approximates the true geodesic update $\text{Retract}_{\mathbf{k}}(\mathbf{V}) = \exp_{\mathbf{k}}(\mathbf{V}) + O(||\mathbf{V}||^2)$. This preserves the constraint $\mathbf{k}^\dagger \mathbf{k} = \mathbf{I}_u$. Common retraction methods include QR-based, polar-based, Cayley transform, and the exponential map. QR-based retractions use a first-order approximation, polar and Cayley methods are second-order, and the exponential map is the exact one. See Tab. 1 for more detail. Here, we apply Cayley method for our work.

Finally, during optimization, \mathbf{k} moves along the geodesic $\gamma(\tau)$ to the optimal point \mathcal{E} . See Fig. 12 for an illustration.

References

1. Chuang, I. L. & and, M. A. N. Prescription for experimental determination of the dynamics of a quantum black box. *J. Mod. Opt.* **44**, 2455–2467, DOI: [10.1080/09500349708231894](https://doi.org/10.1080/09500349708231894) (1997).
2. Poyatos, J. F., Cirac, J. I. & Zoller, P. Complete characterization of a quantum process: The two-bit quantum gate. *Phys. Rev. Lett.* **78**, 390–393, DOI: [10.1103/PhysRevLett.78.390](https://doi.org/10.1103/PhysRevLett.78.390) (1997).
3. Nielsen, M. A. & Chuang, I. L. *Quantum Computation and Quantum Information* (Cambridge University Press, 2000).
4. O'Brien, J. L. *et al.* Quantum process tomography of a controlled-not gate. *Phys. Rev. Lett.* **93**, 080502, DOI: [10.1103/PhysRevLett.93.080502](https://doi.org/10.1103/PhysRevLett.93.080502) (2004).
5. Riebe, M. *et al.* Process tomography of ion trap quantum gates. *Phys. Rev. Lett.* **97**, 220407, DOI: [10.1103/PhysRevLett.97.220407](https://doi.org/10.1103/PhysRevLett.97.220407) (2006).
6. Tinkey, H. N., Meier, A. M., Clark, C. R., Seck, C. M. & Brown, K. R. Quantum process tomography of a mølmer-sørensen gate via a global beam. *Quantum Sci. Technol.* **6**, 034013, DOI: [10.1088/2058-9565/ac0543](https://doi.org/10.1088/2058-9565/ac0543) (2021).
7. Bialczak, R. C. *et al.* Quantum process tomography of a universal entangling gate implemented with josephson phase qubits. *Nat. Phys.* **6**, 409–413, DOI: [10.1038/nphys1639](https://doi.org/10.1038/nphys1639) (2010).
8. Xiao, S., Wang, Y., Dong, D. & Zhang, J. Two-stage solution of quantum process tomography

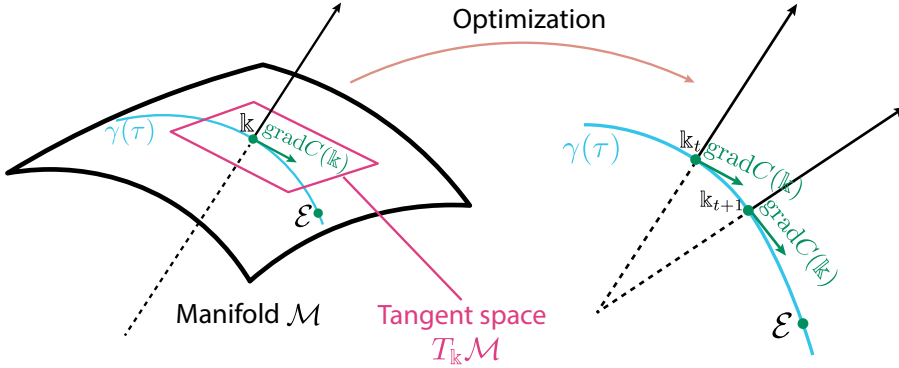


Figure 12. Illustration of the Riemannian optimization.

Retraction Method	Order	Description	Complexity	Pros	Cons
QR-based	First	Uses QR decomposition to project onto the manifold.	$\mathcal{O}(n^3)$ (QR)	Simple, efficient.	Lower accuracy.
Polar-based	Second	Uses polar decomposition for retraction.	$\mathcal{O}(n^3)$ (SVD)	Higher accuracy.	More expensive than QR.
Cayley Transform	Second	Uses Cayley transform to approximate the exponential map.	$\mathcal{O}(n^3)$ (Matrix inverse)	Preserves structure, works well for Lie groups.	Requires stability.
Exponential Map	Exact	Computes the matrix exponential along the geodesic.	$\mathcal{O}(n^3)$ (Matrix exp)	Most accurate.	Computationally expensive.

Table 1. Comparison of retraction methods in Riemannian optimization.

in the natural basis. In *2022 IEEE 61st Conference on Decision and Control (CDC)*, 5807–5812, DOI: [10.1109/CDC51059.2022.9992920](https://doi.org/10.1109/CDC51059.2022.9992920) (2022).

9. Quiroga, D. A. & Kyrillidis, A. Using non-convex optimization in quantum process tomography: Factored gradient descent is tough to beat. In *2023 IEEE International Conference on Rebooting Computing (ICRC)*, 1–10, DOI: [10.1109/ICRC60800.2023.10386455](https://doi.org/10.1109/ICRC60800.2023.10386455) (2023).
10. Shabani, A. *et al.* Efficient measurement of quantum dynamics via compressive sensing. *Phys. Rev. Lett.* **106**, 100401, DOI: [10.1103/PhysRevLett.106.100401](https://doi.org/10.1103/PhysRevLett.106.100401) (2011).
11. Xue, S. *et al.* Efficient quantum process tomography for clifford circuits. *Phys. Rev. A* **108**, 032419, DOI: [10.1103/PhysRevA.108.032419](https://doi.org/10.1103/PhysRevA.108.032419) (2023).

12. Ahmed, S., Quijandría, F. & Kockum, A. F. Gradient-descent quantum process tomography by learning kraus operators. *Phys. Rev. Lett.* **130**, 150402, DOI: [10.1103/PhysRevLett.130.150402](https://doi.org/10.1103/PhysRevLett.130.150402) (2023).
13. Volya, D., Nikitin, A. & Mishra, P. Fast quantum process tomography via riemannian gradient descent (2024). [2404.18840](https://arxiv.org/abs/2404.18840).
14. Wiersema, R. & Killoran, N. Optimizing quantum circuits with riemannian gradient flow. *Phys. Rev. A* **107**, 062421, DOI: [10.1103/PhysRevA.107.062421](https://doi.org/10.1103/PhysRevA.107.062421) (2023).
15. Torlai, G. *et al.* Quantum process tomography with unsupervised learning and tensor networks. *Nat. Commun.* **14**, 2858, DOI: [10.1038/s41467-023-38332-9](https://doi.org/10.1038/s41467-023-38332-9) (2023).
16. Xue, S. *et al.* Variational quantum process tomography of unitaries. *Phys. Rev. A* **105**,

032427, DOI: [10.1103/PhysRevA.105.032427](https://doi.org/10.1103/PhysRevA.105.032427) (2022).

17. Hai, V. T. & Ho, L. B. Universal compilation for quantum state tomography. *Sci. Reports* **13**, 3750, DOI: [10.1038/s41598-023-30983-4](https://doi.org/10.1038/s41598-023-30983-4) (2023).
18. Tuan Hai, V. *et al.* Multi-target quantum compilation algorithm. *Mach. Learn. Sci. Technol.* **5**, 045057, DOI: [10.1088/2632-2153/ad9705](https://doi.org/10.1088/2632-2153/ad9705) (2024).
19. Heya, K., Suzuki, Y., Nakamura, Y. & Fujii, K. Variational quantum gate optimization (2018). [1810.12745](https://arxiv.org/abs/1810.12745).
20. Khatri, S. *et al.* Quantum-assisted quantum compiling. *Quantum* **3**, 140, DOI: [10.22331/q-2019-05-13-140](https://doi.org/10.22331/q-2019-05-13-140) (2019).
21. Volkoff, T., Holmes, Z. & Sornborger, A. Universal compiling and (no-)free-lunch theorems for continuous-variable quantum learning. *PRX Quantum* **2**, 040327, DOI: [10.1103/PRXQuantum.2.040327](https://doi.org/10.1103/PRXQuantum.2.040327) (2021).
22. Hai, V. T., Viet, N. T. & Ho, L. B. $\langle qo|op \rangle$: A quantum object optimizer. *SoftwareX* **26**, 101726, DOI: <https://doi.org/10.1016/j.softx.2024.101726> (2024).
23. Bouchard, F. *et al.* Quantum process tomography of a high-dimensional quantum communication channel. *Quantum* **3**, 138, DOI: [10.22331/q-2019-05-06-138](https://doi.org/10.22331/q-2019-05-06-138) (2019).
24. Granade, C., Ferrie, C. & Flammia, S. T. Practical adaptive quantum tomography*. *New J. Phys.* **19**, 113017, DOI: [10.1088/1367-2630/aa8fe6](https://doi.org/10.1088/1367-2630/aa8fe6) (2017).
25. Christandl, M., König, R. & Renner, R. Postselection technique for quantum channels with applications to quantum cryptography. *Phys. Rev. Lett.* **102**, 020504, DOI: [10.1103/PhysRevLett.102.020504](https://doi.org/10.1103/PhysRevLett.102.020504) (2009).
26. Rodionov, A. V. *et al.* Compressed sensing quantum process tomography for superconducting quantum gates. *Phys. Rev. B* **90**, 144504, DOI: [10.1103/PhysRevB.90.144504](https://doi.org/10.1103/PhysRevB.90.144504) (2014).
27. Gaikwad, A., Shende, K., Arvind & Dorai, K. Implementing efficient selective quantum process tomography of superconducting quantum gates on ibm quantum experience. *Sci. Reports* **12**, 3688, DOI: [10.1038/s41598-022-07721-3](https://doi.org/10.1038/s41598-022-07721-3) (2022).
28. Lee, S. M., Park, H. S., Lee, J., Kim, J. & Bang, J. Quantum state learning via single-shot measurements. *Phys. Rev. Lett.* **126**, 170504, DOI: [10.1103/PhysRevLett.126.170504](https://doi.org/10.1103/PhysRevLett.126.170504) (2021).
29. Tagare, H. D. Notes on optimization on stiefel manifolds (2011).
30. Mezzadri, F. How to generate random matrices from the classical compact groups (2007). [math-ph/0609050](https://arxiv.org/abs/math-ph/0609050).
31. Surawy-Stepney, T., Kahn, J., Kueng, R. & Guta, M. Projected Least-Squares Quantum Process Tomography. *Quantum* **6**, 844, DOI: [10.22331/q-2022-10-20-844](https://doi.org/10.22331/q-2022-10-20-844) (2022).
32. Šafránek, D. Simple expression for the quantum fisher information matrix. *Phys. Rev. A* **97**, 042322, DOI: [10.1103/PhysRevA.97.042322](https://doi.org/10.1103/PhysRevA.97.042322) (2018).

Acknowledgments (not compulsory)

This paper is supported by JSPS KAKENHI Grant No.23K13025.

Author contributions statement

H.L.D.L. developed the computational code and conducted simulations. V.T.H. supervised the coding process and guided its implementation. L.B.H. formulated the theoretical framework and designed the methodology. All authors contributed to the analysis, discussion, and manuscript preparation.